Selective laser melting of Ti–35Nb composite from elemental powder mixture: Microstructure, mechanical behavior and corrosion behavior

J.C. Wang[a,b], Y.J. Liu[b], P. Qin[a], S.X. Liang[a], T.B. Sercombe[b,**], L.C. Zhang[a,*]

[a] School of Engineering, Edith Cowan University, 270 Joondalup Drive, Joondalup, Perth, WA, 6027, Australia
[b] School of Mechanical and Chemical Engineering, M050, The University of Western Australia, 35 Stirling Highway, Crawley, Perth, WA, 6009, Australia

ARTICLE INFO

ABSTRACT

The availability of alloyed powder feedstock and chemical inhomogeneity, which often occur when using elemental mixed powder, have been long-term concerns of selective laser melting (SLM) of metallic materials. In this work, a Ti–35Nb alloy (in wt.%) was manufactured using SLM from elemental mixed powder to study the microstructure, mechanical behavior, and corrosion properties of the resultant parts. Microstructural characterizations show that the SLM-produced Ti–35Nb is composed of fine near β phase dendrites and undissolved Nb particles, which produces in a relatively low Young's modulus (84.7 ± 1.2 GPa). The chemical homogeneity and microstructural homogeneity are improved by heat treatment, resulting in a more homogeneous microstructure and smaller Nb particles. The undissolved large Nb particles play an important role in the overall performance of the SLM-produced materials, because the boundaries of undissolved large Nb particles in the as-SLMed part act as initiation sites for slip bands. The compressive fracture mechanism illustrates the propagation, arrest and merge of shear bands, thereby revealing the effects on the yield strength and plasticity. The electrochemical experiments show the stable corrosion resistance of as-SLMed sample and the improved corrosion resistance of the heat-treated counterparts. This work sheds insight into the SLM of Ti–Nb powder mixtures for biomedical applications. In particular, the relatively low cost and easy manufacture of elemental powder as feedstock offer significant advantages to the additive manufacturing industry.

1. Introduction

Titanium alloys are considered as one of the important biomaterials for hard-tissue biomedical implants and devices due to their relatively low modulus [1], excellent biocompatibility [2,3], and good corrosion resistance [4–6]. Among all types of titanium alloys, the β-type alloys are regarded as the next generation of implant materials in surgical applications due to the low modulus, which is close to that of human bones [7,8]. It is well known that the large difference in elastic modulus between a surgical implant and the adjacent bones can cause stress-shielding in the bone, which can lead to bone resorption and implant loosening [9–11]. Developing materials with an elastic modulus close to that of bones is known to be an effective solution to minimize stress-shielding and thus to increase implant service life. The recent development of β-type titanium alloys in the Ti–Nb alloy system has led to the rapid progress of low-modulus biomedical materials [12]. For example, the β-type Ti–24Nb–4Zr–8Sn (Ti2448) [13–15], Ti–29Nb–13Ta-4.6Zr (TNTZ) [16] and Ti–45Nb [17] alloys (all in wt.%, the same

hereafter) with good biocompatibility and low elastic modulus (40–70 GPa) have been developed for biomedical applications. The reason for the lower elastic modulus in the β phase (than in the α phase) is attributed to the less dense packing of the atoms in the body-centered cubic (bcc) β phase lattice compared with that in the hexagonal close-packed (hcp) α phase [18]. Besides its excellent cold formability and weldability, Nb, as an excellent β phase stabilizer, plays a significant role in reducing the elastic modulus [19] and in improving the corrosion resistance [20] of Ti-based alloys. In addition, the Nb has a relatively lower melting temperature than other β phase stabilizers, such as V, Ta, and Mo, resulting in less consumption of energy. Furthermore, both vitro and vivo tests have shown that the addition of biocompatible and non-toxic Nb into Ti-based alloy could improve the adhesion and proliferation of bone tissues [21–23].

Conventional techniques, such as spark plasma sintering [24,25], pressure-less sintering [24], and free forging [25] have been widely explored to manufacture Ti–Nb mixed powder composites. However, when manufacturing complex structured components, these traditional
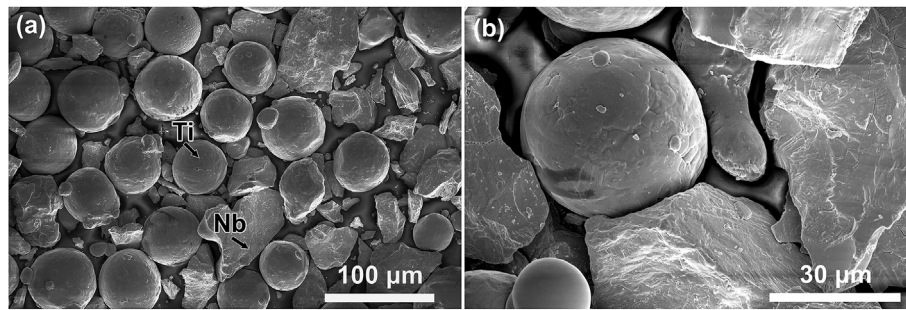
Fig. 1. SEM images of the Ti–35Nb powder mixture of CP-Ti powder and Nb powder at (a) low, and (b) high magnification. The titanium particles are nearly spherical, while the Nb is irregular.

methods have significant limitations, such as high material wastage and multi-step post processing [26]. Recently, additive manufacturing (AM), such as selective laser melting (SLM) [6,27–29] and electron beam melting [30,31] have emerged as methods to produce components through a layer-by-layer process directly from CAD models by selectively full melting and consolidating the starting powder. The superiority of the AM is that it advances the development of manufacturing and biomedical engineering, via its capability to fast manufacture lightweight, complex-structured automotive, and aerospace parts [32,33], as well as patient-specific implants [34–36]. Furthermore, AM facilitates a new path for producing novel β-type composites by in situ alloying elemental powder mixtures [37–42]. Recent reports demonstrate that the properties and microstructure of SLM-produced parts could be much improved by tuning particle size [43], heat treatment [19,24,44], chemical composition [20] and manufacturing process variables [17,45,46].

Although some work has been conducted on the manufacturing of β titanium matrix composites using Ti–Nb elemental powder mixtures, there are still problems on how to obtain a homogeneous β phase microstructure, which primarily results from the large difference in particle size, melting point and density between these two metallic elements [20,25,45,47,48]. For example, a large difference in melting temperature could induce undissolved particles; variance in density could lead to the segregation and inhomogeneity during melting and solidification in the SLM process [45,47]. In particular, the density and melting point of Nb (8.6 g/cm³, 2468 °C) are about 2 and 1.4 times respectively to the corresponding ones for Ti (4.5 g/cm³, 1668 °C). Such a large difference in both density and melting point would be an obstacle in the SLM process as well as in other powder metallurgy technologies. Oliveira et al. [48] studied the sintered porous Ti–35Nb composites which contained undissolved Nb and found that their moduli are in the range of elastic moduli of human bones. Bahador et al. [25] investigated the consolidation of an elemental mixture of Ti-36.7Nb using spark-plasma sintering and found that inhomogeneous microstructure with randomly distributed undissolved Nb particles is formed. Yılmaz et al. [20] studied the mixed powder of Ti–27Nb, Ti–43Nb, and Ti-56.4Nb under powder injection molding technology. Their results showed an increased chemical inhomogeneity, porosity and corrosion resistance with increasing the Nb content. Zhuravleva et al. [23] compared the SLM-produced and hot-pressing Ti–40Nb alloys using ball-milled powder mixtures, suggesting both samples have a high-porosity level of microstructure. The SLM-produced Ti-25.5Nb, Ti-39.3Nb [47] and Ti-40.5Nb [45,47] using elemental powder mixtures show chemical and microstructural inhomogeneity. Therefore, in order to take advantage of the lower cost and flexibility offered by elemental powder mixtures, there is a need to optimize the homogeneity of the β phase and to understand the effect of heterogeneity of undissolved Nb on the mechanical and corrosion properties in binary Ti–Nb composites.

As such, this work investigated the SLM-processed binary Ti–35Nb composites produced from the Ti (65 wt%) and Nb (35 wt%) elemental powder mixture. The effects of the microstructure and heterogeneous β

phase on the mechanical properties and fracture mechanisms were systematically studied. The electrochemical measurement in simulated body solution was also performed to facilitate the understanding of the homogeneity on corrosion resistance.

2. Materials and methods

2.1. Materials preparation

Commercially titanium and niobium powder were chosen as precursor feedstock. The gas-atomized commercially pure titanium (CP–Ti) powder (Grade 1, Advanced Powders and Coatings, Canada) was in a spherical shape with particle size of 40–65 μm. The niobium powder (Sophia's Wholesale, China) was irregular in shape with particle size of 60–95 μm. The elemental titanium powder and niobium powder were mixed in a weight percentage of 65:35 (i.e. Ti-35 wt%Nb). The powder mixture was then mixed in a Turbula T2F mixer for 1 h. The morphologies of simply mixed powder of Ti and Nb are shown in Fig. 1, which shows that the Ti powder was nearly spherical and uniform in size while the Nb powder was irregular in shape with sharp edges and had a wide particle size distribution.

The particle size distribution of the Ti–35Nb powder mixture was analyzed by MASTERSIZER 2000 (Malvern, UK). Fig. 2(a) and (b) show the particle size distribution of the CP-Ti powder and Nb powder, respectively. As seen from the figures, the CP-Ti powder and Nb powder had a $d_{50} = 63.45$ μm and $d_{50} = 74.17$ μm, respectively. Fig. 2(c) shows the particle size distribution of Ti–35Nb elemental powder mixture, which had a $d_{10} = 39.52$ μm, $d_{50} = 67.05$ μm, and $d_{90} = 341.06$ μm. Fig. 2(d) contains the energy dispersive spectroscopy (EDS) results of the Ti–35Nb powder mixture, from which the chemical composition of the powder mixture was measured to be 64.3 wt% Ti and 35.7 wt% Nb.

2.2. Sample preparation and heat treatment

A Realizer SLM-100 selective laser melting machine (Germany) was used to manufacture cubic samples with dimension of $7 \times 7 \times 7$ mm³, cylindrical samples with diameter 6 mm and length 12 mm and with diameter 9 mm and length 60 mm. The SLM machine had a 200 W, 1.064 μm fibre laser (Yb:YAG). The build chamber was purged with high purity Ar and the oxygen content was maintained below 0.1% to minimize oxidation [49]. Table 1 summarizes the SLM processing parameters, from which the resultant energy density (E) can be estimated. Generally, the E is a simplified value that indicates the laser energy over the selected volume of bulk powder in a single layer. The laser energy density (E, in J/mm³) was calculated using Eq. (1) [49–51]:

$$E = \frac{P}{v \cdot t \cdot s} \tag{1}$$

where P is the laser power (W), v is the laser scan speed (mm/s), t is the layer thickness (mm), and s is the hatch space (mm). Based on Eq. (1),
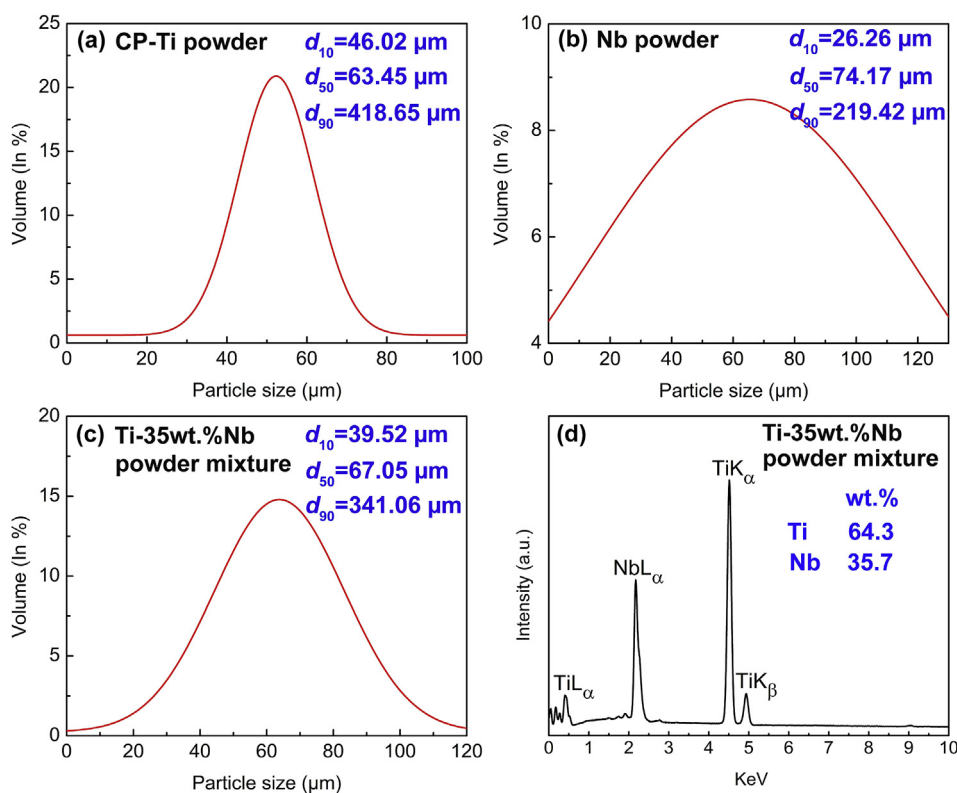
Fig. 2. Particle size distribution of (a) CP-Ti powder, (b) Nb powder and (c) Ti–35Nb powder mixture; and (d) the chemical composition of Ti–35Nb elemental powder mixture.

Table 1
Main SLM processing parameters.

Parameter	Value
Laser power (W)	200
Laser scan speed (mm/s)	500
Laser spot size (μm)	40
Layer thickness (μm)	50
Hatch space (μm)	100
Energy density (J/mm^3)	80

the energy density for this work was estimated to be 80 J/mm^3, which was twice that for SLM-produced Ti–5Cu composite (40 J/mm^3) by taking into account that the melting point of Nb is about twice that of Cu [6].

Considering that the undissolved Nb is the main obstacle for phase and chemical heterogeneity, the diffusion of Nb would improve the chemical homogeneity after heat treatment. The diffusion coefficient of Nb into Ti is very slow and strongly dependent on temperature (range from 800 °C to 1300 °C) and time (5–24 h) [52,53]. In this work, solution treatment was performed for 24 h at 1000 °C [54] in a tube furnace under flowing high purity Ar gas at 0.5 L/min, and then air cooled. The relative density of SLM-produced Ti–35Nb was evaluated as 98.1 ± 0.83% by the Archimedes principle. After the heat treatment (1000 °C), the measured relative density was same as the SLM-produced sample.

2.3. Mechanical testing

The mechanical behavior of SLM-produced Ti–35Nb was evaluated by uniaxial compression testing. The ASTM E9-09 standard was referenced for preparing the compressive test specimens and conducting tests. The outer surface and both end faces of the SLM-produced cylindrical specimens were ground by silicon carbide papers up to 2000

grits to ensure smooth and flat surfaces [55,56]. Each cylindrical specimen had a height to diameter ratio of approximately 1.7 (~9.2 mm in length and 5.4 mm in diameter). An Instron 5982-universal machine (maximum capacity 100 kN) was used to conduct compression tests at a constant strain rate of 0.5 mm/min. The compression test loading direction was parallel to the build direction for all the three samples. The compressive yield strength and plastic strain was calculated using the 0.2% offset method from the measured engineering stress-strain curves. The ultrasonic velocity method was used to measure the Young's modulus at room temperature using RFDA basic (IMCE NV, Belgium). Three samples (diameter 9 mm × length 60 mm) were measured based on the ASTM E1876-15 standard for the Young's modulus. Vickers micro-hardness measurements were conducted on mirror polished surfaces using a load of 5 kgf and a dwell time 20 s.

2.4. Characterizations

X-ray diffraction (XRD, PANalytical Empyrean, Netherlands) with Cu-Kα radiation (wavelength λ = 0.15406 nm) was used to characterize the constituent phases in SLM-produced Ti–35Nb alloy. The scanning angle (2θ) was between 30° and 80° at 40 kV and 40 mA and a scan rate was 0.4°/s. The microstructure and surface morphology were characterized using scanning electron microscopy (SEM, FEI Verios XHR 460) at 20 kV [28]. The chemical composition, surface morphologies, and microstructure of all samples were examined using SEM attached with energy dispersive spectroscopy (EDS, Aztec). Samples for microstructure characterisation were polished using standard metallographic techniques and finished with 0.05 μm colloidal silica.

2.5. Electrochemical measurements

Electrochemical tests of the Ti–35Nb samples were conducted in a beaker containing 3.5 wt% NaCl solution (NaCl: Purity ≥ 99.5%, CAS No. 7647-14-5, Sigma-Aldrich) at room temperature. All
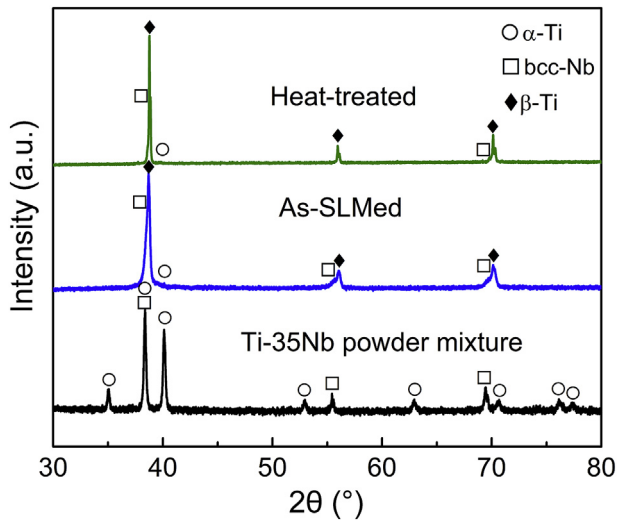
Fig. 3. XRD patterns of the elemental powder mixture, as-SLMed, and heat-treated Ti–35Nb composite samples.

electrochemical measurements were undertaken by a conventional three-electrode cell, which connected to a Luggin capillary bridge. The three-electrode cell consisted of a working electrode (test sample), a counter electrode (platinum net), and a saturated calomel electrode (SCE) (reference electrode) [57]. The area of the sample that was exposed to the electrolye was approximately 36 mm^2. After being immersed in NaCl solution for 3600 s to acquire a stabilized open circuit potential (OCP). The potentiodynamic polarization measurement, from -0.25 V (vs OCP) to $+0.6$ V, was performed at a scan rate of 1 mV/s in an electrochemical workstation (PARSTAT 2273, Princeton Applied Research). The electrochemical impedance spectroscopy (EIS) was performed at an AC amplitude of 10 mV over the scanning frequency range between 0.01 Hz and 100 kHz. All electrochemical results were recorded versus SCE.

3. Results

3.1. Microstructural observations

Fig. 3 shows the XRD patterns of the powder mixture, as-SLMed, and heat-treated Ti–35Nb samples. The mixed Ti–35Nb powder mixture is composed of the respective peaks of the commercially pure Nb powder and pure Ti powder, while both the as-SLMed and heat-treated Ti–35Nb samples comprise of metastable β phase with trace amount of α phase. The Young's modulus of as-SLMed Ti–35Nb sample, measured by ultrasonic method, is 84.7 $\pm$ 1.2 GPa, which is mainly contributed by the β phase. Commercially pure titanium contains a single hcp α phase at ambient temperature and has a melting point at 1668 °C. At a temperature above the β transus temperature (~882.5 °C), Ti undergoes an allotropic transformation to form the bcc β phase [46]. The β↔α transus temperature can be altered by adding sufficient concentration of β stabilizers (e.g. Nb). Indeed, the β phase can even be maintained in a metastable state down to room temperature.

Fig. 4(a) – (c) show backscattered SEM images of the microstructure of the as-SLMed Ti–35Nb sample. It is clear that the as-SLMed sample has higher inhomogeneity than the heat-treated counterpart (Fig. 4(e) and (f)). The chemical compositions of the phase at locations 1 to 7 in Fig. 4 were analyzed by EDS and are summarized in Table 2. The undissolved Nb particles (with an example EDS spectrum in Fig. 4(d)) have the brightest contrast (e.g. points 1 and 5), Ti-rich regions are dark (e.g. point 3), and the Ti–Nb β phases are a moderate grey color (e.g. points 2, 4, 6 and 7). Such a variation in contrast of different phases is a result of the higher atomic number [58] (and therefore greater

backscatter electron intensity) of Nb element (41) than Ti element (22).

As seen in Fig. 4, it is apparent that, at the laser energy density used, the Ti powder is fully melted, but only partial dissolution of the large Nb particles takes place. This is most likely attributed to the much higher melting point of Nb (2468 °C) compared with that of Ti (1668 °C) in the Ti–35Nb powder mixture [47]. It was also reported that the very short laser interaction time and fast cooling rate (10^5–10^8 K/s) [27,59] in the SLM process could contribute to the limited diffusion of large Nb particles into the Ti melt pool. The microstructure before (Fig. 4(b)) and after heat treatment (24 h at 1000 °C) (Fig. 4(e)) as well as their corresponding EDS data (Table 2) are consistent with the microstructural features on XRD results (Fig. 3), where the intensities of β peaks significantly increase and those for the undissolved Nb peaks reduce after heat treatment. Hence, it is evident that the heat treatment has resulted in significant Nb diffusion into Ti (Fig. 4(e)), thereby enhancing the microstructural homogeneity (Fig. 4(f) and (g)) and chemical homogeneity (Fig. 4(h)) of the SLM-produced Ti–35Nb.

3.2. Mechanical behavior

As shown in Fig. 5(a), many wavy slip bands have accumulated around the edges of undissolved Nb particles located at the corners of indenters. Generally, the wave-like slip bands around the indenters indicate that the greater plastic deformation takes place in a material than that of straight slip bands formed in the material [60]. Fig. 5(b) shows a higher magnification image for the dashed frame in (a), which demonstrates that the interface of the large Nb particle and β titanium phase act as the initiation site for slip bands. The large Nb particles can also be simply regarded as stress concentrators. The high local stress near these stress concentrations could facilitate to form slip bands. In contrast, after heat treatment, there are only few slip bands are observed around the undissolved Nb particles, as shown in Fig. 5(c) and its magnified image (Fig. 5(d)) of the corresponding dashed frame. Hence, it appears that the initial large undissolved Nb in the as-SLMed Ti–35Nb sample facilitates slip propagation. However, the heat treatment not only promotes diffusion of the Nb into the Ti, reducing the size of the undissolved Nb particles, but also enhances the solution hardening of Nb and homogeneity of phases. Therefore, the amount of slip band is significantly reduced and slip bands are more homogeneously distributed. It reveals that annealing could effectively improve the chemical homogeneity and cement the bonding of β grains. The measured hardness of the as-SLMed Ti–35Nb (240 $\pm$ 15 HV) is lower than that of the heat-treated (252 $\pm$ 10 HV) counterpart. This result agrees well with other reports where the solid solution hardening of Ti by Nb results in a higher hardness in the Ti–Nb β phase compared with CP-Ti α phases [20,47,48].

Fig. 6 demonstrates that the Ti–35Nb composites have excellent work hardening behavior after yielding and high plasticity under compressive load conditions. The heat-treated Ti–35Nb samples exhibit a lower yield strength of (640 $\pm$ 12 MPa) compared to the as-SLMed counterparts (660 $\pm$ 13 MPa). This suggests that the grain growth occurred during heat treatment (24 h at 1000 °C) does not have a significant detrimental effect on the strength. The as-SLMed sample shows high plasticity (38.5 $\pm$ 1.5%) due to the existence of nearly full β phase, despite of the chemical inhomogeneity. In contrast, after homogenization heat treatment, the sample displays much higher plasticity (47.3 $\pm$ 1.1%). Such an increase in plasticity of the heat-treated sample without compromising yield strength reveals the homogenization process could really enhance the phase bonding. The great dissolution of Nb into Ti matrix could form large number of β Ti–Nb phase, which performs as a strengthener to improve the yield strength and plasticity in the composite [61].

Fig. 7 illustrates the backscattered SEM images of the outer side surface deformation regions at a strain of 15% in order to study the fracture mechanism. Fig. 7(a) and (b) display a large number of deformation bands in the heterogeneous microstructure of the as-SLMed
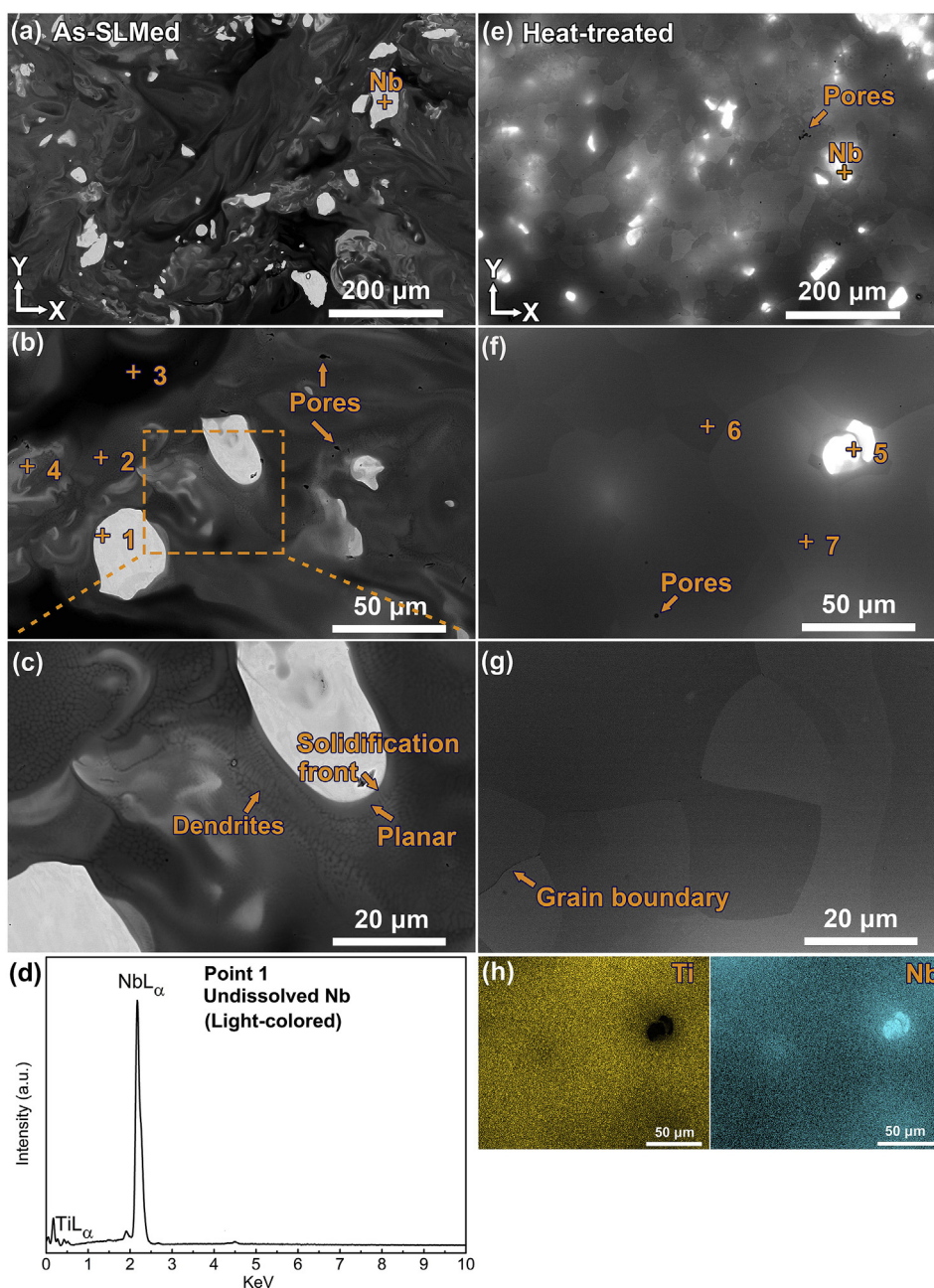
Fig. 4. Backscattered SEM images of cross-sectional microstructures of (a)–(c) as-SLMed Ti–35Nb, and (d) EDS spectrum of undissolved Nb-core particles in (b), and (e)–(g) heat-treated Ti–35Nb (heat treatment at 1000 °C under Ar atmosphere for 24 h, then air cooled), and (h) EDS area mapping in (f).

Table 2
EDS results for points illustrated in Fig. 4(b) and (f).

Point	Area	Ti (wt.%)	Nb (wt.%)
1	Bright color, undissolved Nb	1.1 ± 0.2	98.9 ± 0.2
2	Grey color, Ti–Nb matrix	62.0 ± 1.9	38.0 ± 1.9
3	Dark color, Ti-rich	77.9 ± 1.6	22.1 ± 1.6
4	Grey color, Ti–Nb matrix	55.9 ± 2.7	44.1 ± 2.7
5	Bright color, undissolved Nb	0.2 ± 0.1	99.8 ± 0.1
6	Grey color, Ti–Nb matrix	45.1 ± 1.9	54.9 ± 1.9
7	Grey color, Ti–Nb matrix	68.8 ± 0.4	31.2 ± 0.4

sample after yielding. In addition, some discrete shear bands are observed around the large undissolved Nb particles, indicating that the shear localization is not significant in that region. As illustrated in Fig. 7(c), most shear bands appear to across and subsequently stop at

the (arrest zone) interface of the large undissolved Nb-core particles and Ti–Nb matrix. This suggests that the rapid propagation of shear bands is hindered around the large undissolved Nb (arrest zone). Accordingly, the arrest zone of shear bands plays a major role in blocking plastic deformation and shear localization. This agrees well with the compressive testing results (as shown in Fig. 6), i.e. the relatively higher yield strength with good plasticity. In contrast to the as-SLMed Ti–35Nb, the side surface deformation regions in the heat-treated counterpart (Fig. 7(d) – (f)) shows weaved shear bands, which are more evenly distributed across the entire surface. In addition, the smaller Nb particles in the heat-treated Ti–35Nb become invisible after compression.

3.3. Electrochemical performance

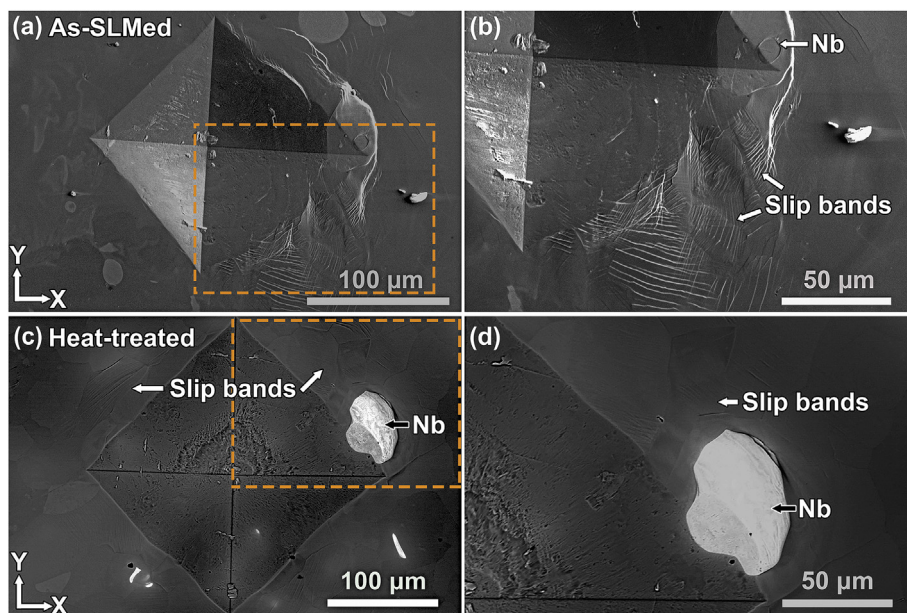As illustrated in Fig. 8, the potentiodynamic polarization curves and

Fig. 5. Backscattered SEM microstructures around a Vickers indent for (a) as-SLMed, and (c) heat-treated Ti–35Nb. Magnified images of (a) and (c) in given dash frames are shown in (b) and (d), respectively.
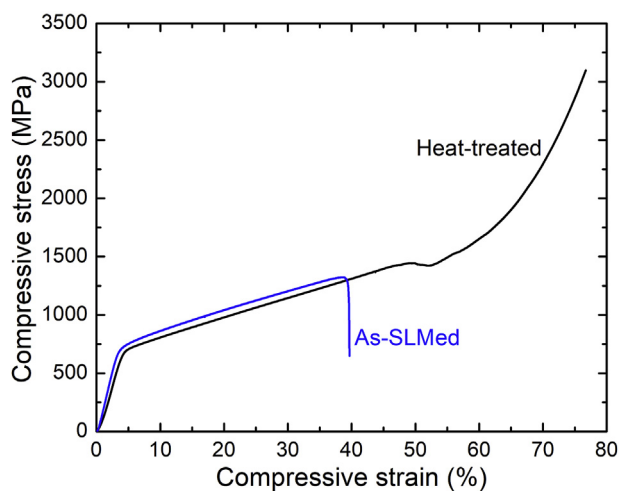

Fig. 6. The compressive engineering stress-strain curves of as-SLMed and heat-treated Ti–35Nb samples.

EIS measured values were recorded after observing the relatively stable open circuit potential (OCP) of the as-SLMed and heat-treated Ti–35Nb samples. Fig. 8(a) displays the OCP for SLM-produced Ti–35Nb samples immersed in 3.5 wt% NaCl solution at room temperature before potentiodynamic polarization tests. Both OCP curves show a similar change trend and shift to more positive value over time. Within the first 1200 s, the reduction of OCP suggests the dissolution phase (Ti and Nb ions) [5,6,62] of the active metal immersed in the solution. While the cationic metal ions gradually reach a critical point in the test solution, the OCP reduces to its lowest value. Beyond this point, the OCP increases, indicating the quick formation of passive films through fast electron transfer at the surface [6,20]. The continued electron transfer between the matrix surface and NaCl solution promotes the thickening of protective passivation film on the surface [6,20], which makes the OCP curves becomes relatively stable at 3600 s. The protective and stable passivation layers are primarily developed by chemical reactions of the Ti and Nb, in which the dissolved ions are gradually hydrated or oxidized into TiO_2, NbO, NbO_2, Nb_2O_5, and $NaNbO_3$ (Eqs. (2)–(7)) [5,6,63–66].

$$Ti^{4+} + 6Cl^- \rightarrow TiCl_6^{2-} \tag{2}$$

$$TiCl_6^{2-} + 2H_2O \rightarrow TiO_2 + 6Cl^- + 4H^+ \tag{3}$$

$$Nb + H_2O \rightarrow NbO + 2H^+ + 2e^- \tag{4}$$

$$NbO + H_2O \rightarrow NbO_2 + 2H^+ + 2e^- \tag{5}$$

$$2NbO + H_2O \rightarrow Nb_2O_5 + 2H^+ + 2e^- \tag{6}$$

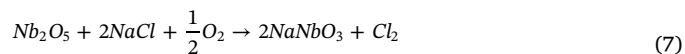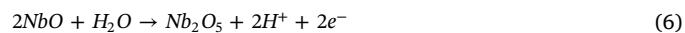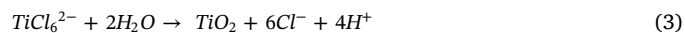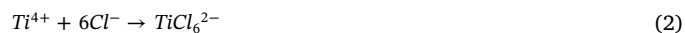$$Nb_2O_5 + 2NaCl + \frac{1}{2}O_2 \rightarrow 2NaNbO_3 + Cl_2 \tag{7}$$

Fig. 8(b) shows the potentiodynamic polarization curves of the samples. The values of corrosion potential of as-SLMed and heat-treated Ti–35Nb samples are approximately at −0.55 V and −0.46 V, respectively, which confirms that the heat-treated Ti–35Nb has a higher corrosion resistance than the as-SLMed counterpart. The electrochemical impedance spectroscopy (EIS) data of measured Ti–35Nb at NaCl solution (3.5 wt%) is shown in the form of Nyquist and Bode magnitude plots (Fig. 8(c) and (d)). The EIS Nyquist plot is usually used to study the resistance of electron transfer. A larger semi-circular arc radius on the Nyquist curve represents a higher corrosion resistance [6]. As can be seen in the Nyquist curve (Fig. 8(c)), typical capacitive arcs are observed. The semi-cicular arc radius of heat-treated Ti–35Nb sample is slightly larger than that of as-SLMed sample, showing that the passivation film has a higher polarization resistance on the metal surface and a more noble corrosion resistance [10,66–68]. It is clear from the Bode-phase plot in Fig. 8(d) that a wide portion of the curves is almost flat in the low and middle frequency ranges, which is the characteristics response of formation of passive film [64]. In general, a wide plateau at a phase angle greater than 70° over a large frequency ranges indicates a higher electron transfer capacity and a high the phase angle closer to 90° signifies a denser oxide film [69]. The Bode-phase angle plots in Fig. 8(d) demonstrate a wide plateau with phase angles close to 90° in the middle to low frequency region, further confirming the highly capacitive behavior of passive film [64,67] of both samples.

4. Discussion

4.1. Microstructural features

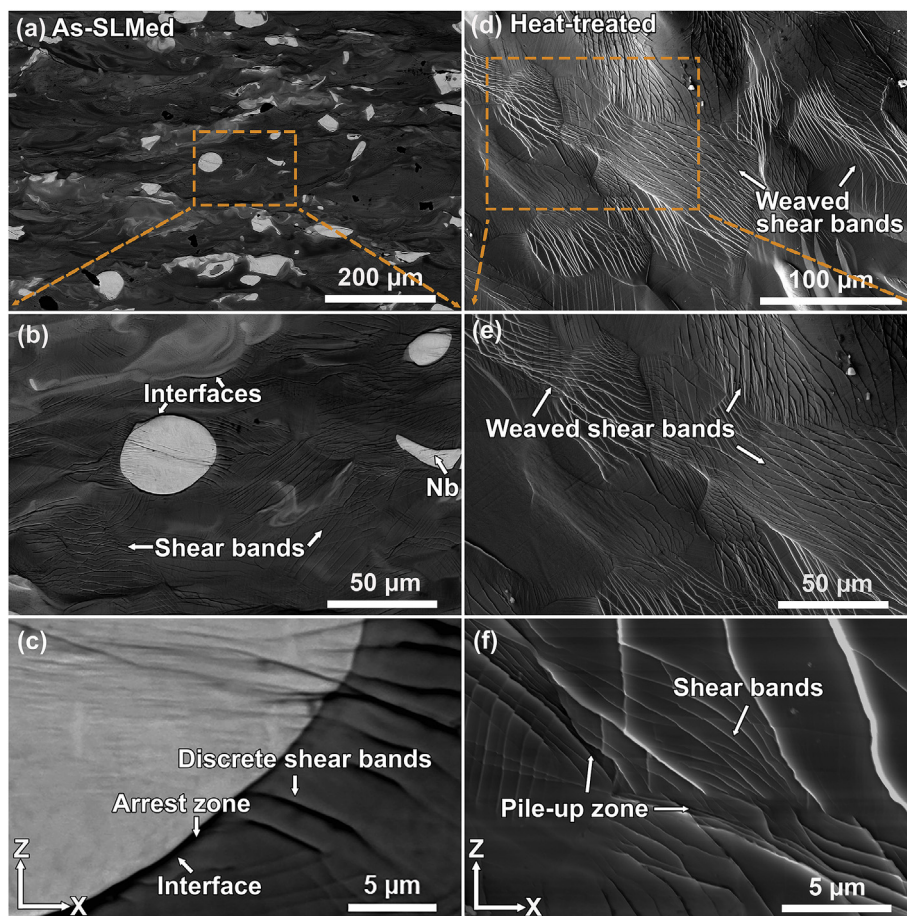It is well known that the amount of the alloying elements and the

Fig. 7. Backscattered SEM microstructures of the outer side surface deformation regions of: (a)–(c) as-SLMed and (e)–(f) heat-treated Ti–35Nb after undergoing 15% strains.
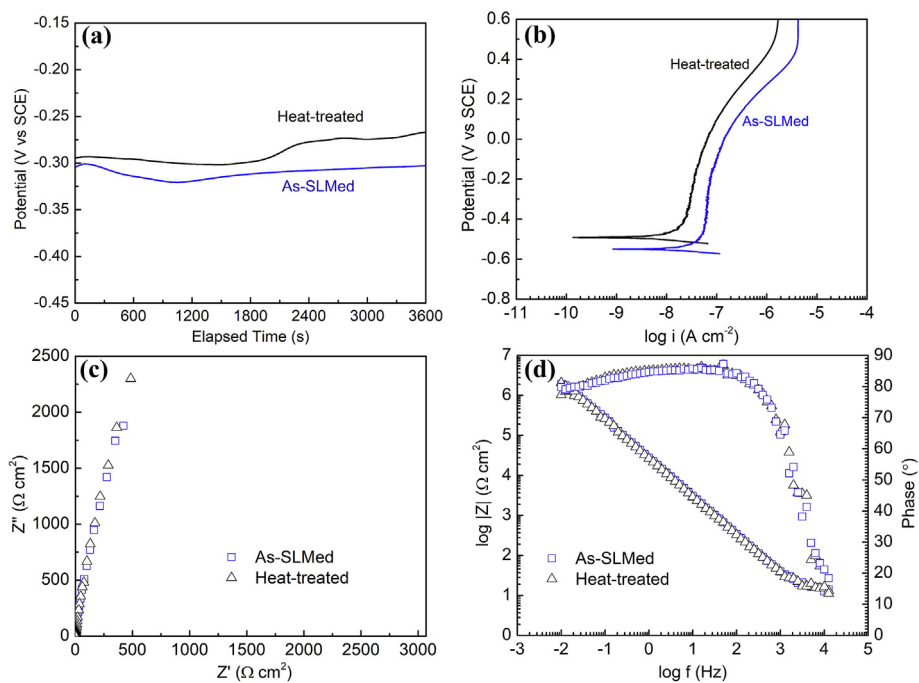

Fig. 8. Electrochemical measurement of the as-SLMed and heat-treated Ti–35Nb in 3.5 wt% NaCl solution at room temperature: (a) The open circuit potential as function of time, (b) the potentiodynamic polarization curve, and the EIS results in the form of (c) nyquist plots and (d) bode plots.

heat treatment temperature determine the stability of β phase [37]. The empirical Molybdenum equivalency (Mo_{eq}), which is the equivalent amount of Mo required to produce the same degree of β stabilization for a given alloy [37], can be used to predict the combined effect of β stabilizing elements. The actual Mo_{eq} of an alloy depends on the alloying elements and their concentration, as shown in Eq. (8). With an increase in the Mo_{eq} value, the stability of the β phase increases. In particular, it takes about 10% molybdenum (Mo_{eq}) to stabilize the fully β phase during quenching [70].

$$Mo_{eq} = 1.0Mo + 0.67V + 0.44W + 0.28Nb + 0.22Ta + 1.6Cr + \dots$$
$$-1.0Al \, [wt. \%] \tag{8}$$

Based on Eq. (8), the Molybdenum equivalence of Ti–35Nb alloy is 9.8%, which is very close to the required the 10% which results in a fully β phase structure. As shown in Fig. 3, the XRD result of the as-SLMed Ti–35Nb powder mixture indicates the almost completely metastable β phase.

It was reported [71] that a relatively higher thermal gradient (G) and lower solidification rate (R) (i.e. very high G/R ratio) would facilitate the formation of planar grains, while a high to medium G/R ratio would induce cellular and columnar dendritic microstructures. The growth of planar grains, which form as a result of the high heat transfer profile and rapid solidification of molten pool during SLM manufacturing, are observed along the solidification front (solid/liquid interface) in the Ti–Nb matrix (in Fig. 4(c)). On one hand, Nb has higher thermal conductivity (54 W/mK) than Ti (21.9 W/mK) [46], which leads to quicker heat dissipation around the undissolved Nb particles than in the Ti–Nb matrix, thereby resulting in a higher thermal gradient (G). On the other hand, the partially undissolved Nb particles (in solid state with high thermal conductivity) have a great effect on solidification rate (R) by acting as the heat sink, which can quickly absorb thermal enegy that is released from the Ti–Nb liquid solution solidifying process. This creates a lower R surrounding the region of solidification front (i.e. the interface between undissolved Nb and Ti–Nb solution) than in the Ti–Nb liquid solution. Hence, the higher G and lower R (i.e. a very high G/R ratio) within the region surrounding the undissolved Nb particles promotes the formation of fine planar grains. In addition, Fig. 4(c) illustrates the dendrites orientated along the boundaries of planar grains. These dendritic grains can be ascribed by the high G/R ratio combined with the increased heterogeneous nucleation sites due to the high content of Nb solute [47]. For the Ti–Nb composites, the liquid can undergo solidification undercooling because of the change of solute (Nb) concentration (as shown in Table 2) caused by solute redistribution (also known as constitutional supercooling) at the solidification front. This leads to a change of the solidification temperature of the liquid phase, which in turn causes the liquid to solidify ahead of the solid-liquid boundary. Such a supercooling phenomenon can induce instability of the solidification front and results in a transition from planar grain growth to dendritic grain growth (Fig. 4(c)) [37]. The diffusion of Nb into the β phase depends on both temperature and time [52,53]; therefore increasing in Nb content would require longer diffusion time. The heat-treated Ti–35Nb sample (Fig. 4(e)) clearly shows the improved homogeneity, where most the undissolved Nb particles have diffused into the Ti–Nb matrix, thereby decreasing both the size and number of the Nb particles. It has been reported that the high volume of Nb (elemental powder) addition into Ti matrix is one of the main reasons to cause high porosity (Fig. 4(b) and (e)) due to the relatively slow diffusion rate of Nb into matrix [20]. Accordingly, Zhuravleva et al. [23] successfully fabricated Ti–40Nb (ball-milled mixed powder) solid cylinders with high porosity and promising strength. Fig. 4(f) shows the refined microstructure as the result of the diffusion of Nb and growth of dendritic grains (Fig. 4(c)). Accordingly, the multiphased Ti–35Nb sample exhibits different physical and chemical properties before and after heat treatment.

4.2. Deformation mechanism

After Vickers hardness testing, there is usually a formation of slip band patterns surrounding the indenter under the effect of dominated normal stress and shear stress [55,72]. Therefore, the micro-hardness measurement can be employed to study the macroscopic elasto-plastic behavior of various materials through analyzing localized plastic deformation patterns [73]. In general, the strain localization around the indenters can generate slip bands, which represent the plastic deformation in that region. In other words, the cumulative number of slip bands surrounding the edge and corner of indenter is directly proportional to the capacity of the material to undergo plastic deformation [60]. Typically, these shear bands are presented as either straight or wavy lines. The straigt slip bands are regular parallel lines, which spread across the indenter edges. The wavy slip bands are normally irregular and rough semicircular bands, which are initiated close to the margin of a indenter and spread over indenter corners. Fig. 5 shows the backscattered SEM images with different slip band patterns for both as-SLMed and heat-treated specimens. The proposed mechanism is that, in the prominently inhomogeneous β phase microstructure in the as-SLMed Ti–35Nb sample, weak bonding [25,74] occurs at interfaces between the large undissolved Nb particles and matrix, which cannot accommodate high plastic strains. The plastic mismatch between the Nb-core and Ti–Nb matrix causes more slip bands.

The β phase alloys have several attractive properties, such as excellent strength to modulus ratio, reasonable fracture toughness [47], and high corrosion resistance [20]. However, the compressive yield and fracture behavior of SLM-produced Ti–Nb composites are still unclear. This is especially true because of their inhomogeneous microstructure, which could lead to instability along the interfaces ((Fig. 7(b)) of the undissolved Nb particles. Based on the aforementioned results, the compressive fracture mechanism of the as-SLMed Ti–35Nb and heat-treated Ti–35Nb composites are proposed. In the early stages of plastic deformation of as-SLMed Ti–35Nb, the Ti–Nb zones (ductile bcc-β-type phase regions) start to yield, and then partial stress is transferred to the surrounding undissolved Nb particles. The undissolved Nb-cores in the as-SLMed Ti–35Nb (Fig. 7(b)) play as stress concentrator for grain boundary sliding. The weak bonding (Fig. 7(c)) between the interfaces of undissolved Nb-cores and dendrites could be easily broken under high compressive stress, leading to a large boundary sliding (i.e. formation of arrest zone) on the matrix. After heat treatment, the large grain boundaries in heat-treated Ti–35Nb (Fig. 7(d)) act as stress concentrators for grain boundary sliding. While the initial shear bands propagate, a new shear band interface is generated by dislocation slip (Fig. 7(e)). The pile-ups of shear bands (Fig. 7(f)) around shear regions then become a high stress concentration zone and merge the shear bands, which can reduce stress concentration, thus improving the plasticity toughness [74].

4.3. Corrosion behavior

Ti–Nb alloys have attracted wide attention in biomedical and marine application due to their excellent corrosion resistance [18]. Ti–Nb alloys have a strong ability to quickly form a stable self-protective oxide film on the metal surface, such as titanium oxide (TiO_2) and niobium oxide (Nb_2O_5). More importantly, they have the ability to self-repair any damage to the film, which prevents further corrosion. The formation of a protective film on the metal surface would certainly improve the surface stability [20,75]. In addition, both Ti–35Nb composites have higher corrosion resistance than the cast CP-Ti (-0.58 V) [75]. The high corrosion resistance can be explained by the formation of niobium oxide film, which is more stable than titanium oxide layer on the surface and more protective for corrosion in a corrosive environment [20,75]. Another possible reason is that the enthalpy of Nb element reaction with oxygen (-1766 kJ/mol) is approximately twice that of Ti (-888.8 kJ/mol), resulting in quicker formation of niobium

oxide film [20]. This suggests that the improved chemical homogeneity and more uniform Nb distribution (Fig. 4(e) – (h) and Table 2) of the heat-treated Ti–35Nb sample are the reason for improved corrosion resistance. By contrast, the slightly lower corrosion resistance of the as-SLMed Ti–35Nb sample than that of heat-treated Ti–35Nb is attributed to the uneven distribution of alloying elements and phases. A better-homogenized surface with evenly distributed alloying elements can enhance the development of passivation film with homogeneous chemical composition. Therefore, the formed oxide layer can efficiently cover the entire surface and reduce the corrosion rate.

5. Conclusions

This work offers the insight into the manufacturing of a Ti–35Nb composite using selective laser melting (SLM) and post heat treatment. It emphasizes the capability of SLM to fabricate alloys from elemental powder mixtures, even suitable for those with a significant difference in melting point. The mixture of Nb (35 wt%) with Ti powder led to the stabilization of β phase as a result of both as a β stablizer and rapid solidification in SLM process. The chemical heterogeneity of Ti-rich, large undissolved Nb, and Ti–Nb β phases of the as-SLMed Ti–35Nb material contributed to the mechanical and chemical instability. Heat treatment can significantly improve the chemical homogeneity therefore the resultant properties. This work provides a significant advance in the understanding of the effect of inhomogeneity and more importantly, presents a different method of synthesizing novel β type composites. The main conclusion can be summarized based on the discussion above:

1. The as-SLMed metastable β-type Ti–35Nb samples with relatively low Young's modulus (84.7 ± 1.2 GPa) have been obtained from Ti and Nb powder mixture. However, the shorter laser interaction time coupled with the fast cooling rate of the SLM process has contributed to insufficient time to produce a homogenous structure. As such, the microstructure is highly heterogeneous and includes undissolved Nb particles.
2. The inhomogeneous microstructure and chemical composition of the as-SLMed Ti–35Nb from powder mixture can be improved by optimized heat treatment.
3. The as-SLMed Ti–35Nb samples show good yield strength (660 ± 13 MPa) and high compressive plasticity (38.5 ± 1.5%) due to the existence of nearly full β phase. After homogenization heat treatment, the material has a slightly lower yield strength (640 ± 12 MPa) but much higher compressive plasticity (47.3 ± 1.1%). This is attributed to the improved chemical homogeneity and solution hardening. The shear bands formed around large undissolved Nb particles play an important role in determining the mechanical performance of the SLM-produced Ti–35Nb.
4. Heat treatment can further enhance the corrosion resistance of as-SLMed Ti–35Nb samples because the improved chemical homogeneity can facilitate the homogeneous formation of titanium oxides and niobium oxides.

Conflicts of interest

The authors declare no conflict of interest.

Contributions

J.C.W., T.B.S., and L.C.Z. conceived the experiments and wrote the manuscript. J.C.W. and Y.J.L. conducted the experiments. J.C.W., Y.J.L., P.Q., S.X.L., T.B.S., and L.C.Z. analyzed the data. All authors reviewed the manuscript.

References

[1] M. Qian, W. Xu, M. Brandt, H.P. Tang, Additive manufacturing and postprocessing of Ti-6Al-4V for superior mechanical properties, MRS Bull. 41 (2016) 775–783 https://doi.org/10.1557/mrs.2016.215.

[2] S. Bose, D. Ke, H. Sahasrabudhe, A. Bandyopadhyay, Additive manufacturing of biomaterials, Prog. Mater. Sci. 93 (2018) 45–111 https://doi.org/10.1016/j.pmatsci.2017.08.003.

[3] A.A. Zadpoor, J. Malda, Additive manufacturing of biomaterials, tissues, and organs, Ann. Biomed. Eng. 45 (2017) 1–11 https://doi.org/10.1007/s10439-016-1719-y.

[4] N. Dai, L.C. Zhang, J. Zhang, Q. Chen, M. Wu, Corrosion behavior of selective laser melted Ti-6Al-4V alloy in NaCl solution, Corros. Sci. 102 (2016) 484–489 https://doi.org/10.1016/j.corsci.2015.10.041.

[5] Y. Chen, J. Zhang, N. Dai, P. Qin, H. Attar, L.C. Zhang, Corrosion behaviour of selective laser melted Ti-TiB biocomposite in simulated body fluid, Electrochim. Acta 232 (2017) 89–97 https://doi.org/10.1016/j.electacta.2017.02.112.

[6] P. Qin, Y. Liu, T. Sercombe, Y. Li, C. Zhang, C. Cao, H. Sun, L.-C. Zhang, Improved corrosion resistance on selective laser melting produced Ti-5Cu alloy after heat treatment, ACS Biomater. Sci. Eng. 4 (2018) 2633–2642 https://doi.org/10.1021/acsbiomaterials.8b00319.

[7] Y.J. Liu, X.P. Li, L.C. Zhang, T.B. Sercombe, Processing and properties of topologically optimised biomedical Ti–24Nb–4Zr–8Sn scaffolds manufactured by selective laser melting, Mater. Sci. Eng., A 642 (2015) 268–278 https://doi.org/10.1016/j.msea.2015.06.088.

[8] N. Hafeez, S. Liu, E. Lu, L. Wang, R. Liu, W. lu, L.-C. Zhang, Mechanical behavior and phase transformation of β-type Ti-35Nb-2Ta-3Zr alloy fabricated by 3D-Printing, J. Alloy. Comp. 790 (2019) 117–126 https://doi.org/10.1016/j.jallcom.2019.03.138.

[9] M. Niinomi, Mechanical properties of biomedical titanium alloys, Mater. Sci. Eng., A 243 (1998) 231–236 https://doi.org/10.1016/S0921-5093(97)00806-X.

[10] P. Qin, Y. Chen, Y.-J. Liu, J. Zhang, L.-Y. Chen, Y. Li, X. Zhang, C. Cao, H. Sun, L.-C. Zhang, Resemblance in corrosion behavior of selective laser melted and traditional monolithic β Ti-24Nb-4Zr-8Sn alloy, ACS Biomater. Sci. Eng. 5 (2019) 1141–1149 https://doi.org/10.1021/acsbiomaterials.8b01341.

[11] Y.J. Liu, Y.S. Zhang, L.C. Zhang, Transformation-induced plasticity and high strength in beta titanium alloy manufactured by selective laser melting, Materialia 6 (2019) 100299 https://doi.org/10.1016/j.mtla.2019.100299.

[12] L.-C. Zhang, L.-Y. Chen, A review on biomedical titanium alloys: recent progress and prospect, Adv. Eng. Mater. 21 (2019) 1801215 https://doi.org/10.1002/adem.201801215.

[13] S.J. Li, T.C. Cui, Y.L. Hao, R. Yang, Fatigue properties of a metastable β-type titanium alloy with reversible phase transformation, Acta Biomater. 4 (2008) 305–317 https://doi.org/10.1016/j.actbio.2007.09.009.

[14] Y.J. Liu, H.L. Wang, S.J. Li, S.G. Wang, W.J. Wang, W.T. Hou, Y.L. Hao, R. Yang, L.C. Zhang, Compressive and fatigue behavior of beta-type titanium porous structures fabricated by electron beam melting, Acta Mater. 126 (2017) 58–66 https://doi.org/10.1016/j.actamat.2016.12.052.

[15] L.C. Zhang, D. Klemm, J. Eckert, Y.L. Hao, T.B. Sercombe, Manufacture by selective laser melting and mechanical behavior of a biomedical Ti–24Nb–4Zr–8Sn alloy, Scripta Mater. 65 (2011) 21–24 https://doi.org/10.1016/j.scriptamat.2011.03.024.

[16] H. Yilmazer, M. Niinomi, M. Nakai, J. Hieda, Y. Todaka, T. Akahori, T. Miyazaki, Heterogeneous structure and mechanical hardness of biomedical β-type Ti–29Nb–13Ta–4.6Zr subjected to high-pressure torsion, J. Mech. Behav. Biomed. Mater. 10 (2012) 235–245 https://doi.org/10.1016/j.jmbbm.2012.02.022.

[17] H. Schwab, K.G. Prashanth, L. Lober, U. Kuhn, J. Eckert, Selective laser melting of Ti-45Nb alloy, Metals 5 (2015) 686–694 https://doi.org/10.3390/met5020686.

[18] Y. Bai, J. Li, S. Li, Y. Hao, X. Zhang, R. Yang, Corrosion behaviour and surface modification of the β-type biomedical Ti-24Nb-4Zr-8Sn alloys, Mater. Technol. 31 (2016) 668–680 https://doi.org/10.1080/10667857.2016.1212586.

[19] H.Y. Kim, Y. Ikehara, J.I. Kim, H. Hosoda, S. Miyazaki, Martensitic transformation, shape memory effect and superelasticity of Ti–Nb binary alloys, Acta Mater. 54 (2006) 2419–2429 https://doi.org/10.1016/j.actamat.2006.01.019.

[20] E. Yılmaz, A. Gökçe, F. Findik, H. Gulsoy, Metallurgical properties and biomimetic HA deposition performance of Ti-Nb PIM alloys, J. Alloy. Comp. 746 (2018) 301–313 https://doi.org/10.1016/j.jallcom.2018.02.274.

[21] E. Eisenbarth, D. Velten, M. Müller, R. Thull, J. Breme, Biocompatibility of β-stabilizing elements of titanium alloys, Biomaterials 25 (2004) 5705–5713 https://doi.org/10.1016/j.biomaterials.2004.01.021.

[22] J.P. Bray, A. Kersley, W. Downing, K.R. Crosse, A.J. Worth, A.K. House, G. Yates, A.R. Coomer, I.W.M. Brown, Clinical outcomes of patient-specific porous titanium

endoprostheses in dogs with tumors of the mandible, radius, or tibia: 12 cases (2013-2016), JAVMA-J. Am. Vet. Med. Assoc. 251 (2017) 566–579 https://doi.org/10.2460/javma.251.5.566.

[23] K. Zhuravleva, M. Bönisch, K.G. Prashanth, U. Hempel, A. Helth, T. Gemming, M. Calin, S. Scudino, L. Schultz, J. Eckert, A. Gebert, Production of porous β-type Ti-40Nb alloy for biomedical applications: comparison of selective laser melting and hot pressing, Materials 6 (2013) 5700–5712 https://doi.org/10.3390/ma6125700.

[24] R. Karre, B.K. Kodli, A. Rajendran, N. J, D.K. Pattanayak, K. Ameyama, S.R. Dey, Comparative study on Ti-Nb binary alloys fabricated through spark plasma sintering and conventional P/M routes for biomedical application, Mater. Sci. Eng., C 94 (2019) 619–627 https://doi.org/10.1016/j.msec.2018.10.006.

[25] A. Bahador, E. Hamzah, K. Kondoh, T.A. Abu Bakar, F. Yusof, H. Imai, S.N. Saud, M.K. Ibrahim, Effect of deformation on the microstructure, transformation temperature and superelasticity of Ti–23 at% Nb shape-memory alloys, Mater. Des. 118 (2017) 152–162 https://doi.org/10.1016/j.matdes.2016.12.048.

[26] L.-C. Zhang, H. Attar, Selective laser melting of titanium alloys and titanium matrix composites for biomedical applications: a review, Adv. Eng. Mater. 18 (2016) 463–475 https://doi.org/10.1002/adem.201500419.

[27] Y.J. Liu, Z. Liu, Y. Jiang, G.W. Wang, Y. Yang, L.C. Zhang, Gradient in microstructure and mechanical property of selective laser melted AlSi10Mg, J. Alloy. Comp. 735 (2018) 1414–1421 https://doi.org/10.1016/j.jallcom.2017.11.020.

[28] Y.J. Liu, S.J. Li, L.C. Zhang, Y.L. Hao, T.B. Sercombe, Early plastic deformation behaviour and energy absorption in porous β-type biomedical titanium produced by selective laser melting, Scripta Mater. 153 (2018) 99–103 https://doi.org/10.1016/j.scriptamat.2018.05.010.

[29] H. Attar, M. Calin, L.C. Zhang, S. Scudino, J. Eckert, Manufacture by selective laser melting and mechanical behavior of commercially pure titanium, Mater. Sci. Eng., A 593 (2014) 170–177 https://doi.org/10.1016/j.msea.2013.11.038.

[30] Y. Liu, S. Li, W. Hou, S. Wang, Y. Hao, R. Yang, T.B. Sercombe, L.-C. Zhang, Electron beam melted beta-type Ti–24Nb–4Zr–8Sn porous structures with high strength-to-modulus ratio, J. Mater. Sci. Technol. 32 (2016) 505–508 https://doi.org/10.1016/j.jmst.2016.03.020.

[31] L.-C. Zhang, Y. Liu, S. Li, Y. Hao, Additive manufacturing of titanium alloys by electron beam melting: a review, Adv. Eng. Mater. 20 (2018) 1700842 https://doi.org/10.1002/adem.201700842.

[32] S.C. Joshi, A.A. Sheikh, 3D printing in aerospace and its long-term sustainability, Virtual Phys. Prototyp. 10 (2015) 175–185, https://doi.org/10.1080/17452759.2015.1111519.

[33] P. Rochus, J.Y. Plesseria, M. Van Elsen, J.P. Kruth, R. Carrus, T. Dormal, New applications of rapid prototyping and rapid manufacturing (RP/RM) technologies for space instrumentation, Acta Astronaut. 61 (2007) 352–359 https://doi.org/10.1016/j.actaastro.2007.01.004.

[34] Y. Liu, J. Padmanabhan, B. Cheung, J. Liu, Z. Chen, B.E. Scanley, D. Wesolowski, M. Pressley, C.C. Broadbridge, S. Altman, U.D. Schwarz, T.R. Kyriakides, J. Schroers, Combinatorial development of antibacterial Zr-Cu-Al-Ag thin film metallic glasses, Sci. Rep. 6 (2016) 26950 https://doi.org/10.1038/srep26950.

[35] J.D. Prince, 3D printing: an industrial revolution, J. Electron. Resour. Med. Libr. 11 (2014) 39–45 https://doi.org/10.1080/15424065.2014.877247.

[36] M. Colaco, D.A. Igel, A. Atala, The potential of 3D printing in urological research and patient care, Nat. Rev. Urol. 15 (2018) 213–221 https://doi.org/10.1038/nrurol.2018.6.

[37] B. Vrancken, L. Thijs, J.P. Kruth, J. Van Humbeeck, Microstructure and mechanical properties of a novel β titanium metallic composite by selective laser melting, Acta Mater. 68 (2014) 150–158 https://doi.org/10.1016/j.actamat.2014.01.018.

[38] Y. Ma, G. Ji, X.P. Li, C.Y. Chen, Z.Q. Tan, A. Addad, Z.Q. Li, T.B. Sercombe, J.P. Kruth, On the study of tailorable interface structure in a diamond/Al12Si composite processed by selective laser melting, Materialia 5 (2019) 100242 https://doi.org/10.1016/j.mtla.2019.100242.

[39] L.C. Astfalck, G.K. Kelly, X.P. Li, T.B. Sercombe, On the breakdown of SiC during the selective laser melting of aluminum matrix composites, Adv. Eng. Mater. 19 (2017) 6 https://doi.org/10.1002/adem.201600835.

[40] Q. Wang, L. Ren, X.P. Li, S.Y. Zhang, T.B. Sercombe, K. Yang, Antimicrobial Cu-bearing stainless steel scaffolds, Mater. Sci. Eng. C-Mater. Biol. Appl. 68 (2016) 519–522 https://doi.org/10.1016/j.msec.2016.06.038.

[41] X.P. Li, C. Kong, T. Becker, T. Sercombe, Investigation of interfacial reaction products and stress distribution in selective laser melted Al12Si/SiC composite using confocal Raman microscopy, Adv. Eng. Mater. 18 (2016) 1337–1341 https://doi.org/10.1002/adem.201600150.

[42] H. Attar, M. Bönisch, M. Calin, L.C. Zhang, K. Zhuravleva, A. Funk, S. Scudino, C. Yang, J. Eckert, Comparative study of microstructures and mechanical properties of in situ Ti–TiB composites produced by selective laser melting, powder metallurgy, and casting technologies, J. Mater. Res. 29 (2014) 1941–1950 https://doi.org/10.1557/jmr.2014.122.

[43] J.H. Martin, B.D. Yahata, J.M. Hundley, J.A. Mayer, T.A. Schaedler, T.M. Pollock, 3D printing of high-strength aluminium alloys, Nature 549 (2017) 365 https://doi.org/10.1038/nature23894.

[44] B. Sun, X.L. Meng, Z.Y. Gao, W. Cai, L.C. Zhao, Effect of annealing temperature on shape memory effect of cold-rolled Ti-16 at.%Nb alloy, J. Alloy. Comp. 715 (2017) 16–20 https://doi.org/10.1016/j.jallcom.2017.04.275.

[45] M. Fischer, D. Joguet, G. Robin, L. Peltier, P. Laheurte, In situ elaboration of a binary Ti-26Nb alloy by selective laser melting of elemental titanium and niobium mixed powders, Mater. Sci. Eng. C-Mater. Biol. Appl. 62 (2016) 852–859 https://doi.org/10.1016/j.msec.2016.02.033.

[46] S.L. Sing, W.Y. Yeong, F.E. Wiria, Selective laser melting of titanium alloy with 50 wt% tantalum: microstructure and mechanical properties, J. Alloy. Comp. 660 (2016) 461–470 https://doi.org/10.1016/j.jallcom.2015.11.141.

[47] Q. Wang, C.J. Han, T. Choma, Q.S. Wei, C.Z. Yan, B. Song, Y.S. Shi, Effect of Nb content on microstructure, property and in vitro apatite-forming capability of Ti-Nb alloys fabricated via selective laser melting, Mater. Des. 126 (2017) 268–277 https://doi.org/10.1016/j.matdes.2017.04.026.

[48] C.S.S. de Oliveira, S. Griza, M.V. de Oliveira, A.A. Ribeiro, M.B. Leite, Study of the porous Ti35Nb alloy processing parameters for implant applications, Powder Technol. 281 (2015) 91–98 https://doi.org/10.1016/j.powtec.2015.03.014.

[49] X.J. Wang, L.C. Zhang, M.H. Fang, T.B. Sercombe, The effect of atmosphere on the structure and properties of a selective laser melted Al–12Si alloy, Mater. Sci. Eng., A 597 (2014) 370–375 https://doi.org/10.1016/j.msea.2014.01.012.

[50] L. Thijs, F. Verhaeghe, T. Craeghs, J.V. Humbeeck, J.-P. Kruth, A study of the microstructural evolution during selective laser melting of Ti–6Al–4V, Acta Mater. 58 (2010) 3303–3312 https://doi.org/10.1016/j.actamat.2010.02.004.

[51] H. Attar, M. Bönisch, M. Calin, L.-C. Zhang, S. Scudino, J. Eckert, Selective laser melting of in situ titanium–titanium boride composites: processing, microstructure and mechanical properties, Acta Mater. 76 (2014) 13–22 https://doi.org/10.1016/j.actamat.2014.05.022.

[52] L.R. Sheppard, A.J. Atanacio, T. Bak, J. Nowotny, K.E. Prince, Bulk diffusion of niobium in single-crystal titanium dioxide, J. Phys. Chem. B 111 (2007) 8126–8130 https://doi.org/10.1021/jp0678709.

[53] A.E. Pontau, D. Lazarus, Diffusion of titanium and niobium in bcc Ti-Nb alloys, Phys. Rev. B 19 (1979) 4027–4037 https://doi.org/10.1103/PhysRevB.19.4027.

[54] A.R.G. Brown, D. Clark, J. Eastabrook, K.S. Jepson, The titanium–niobium system, Nature 201 (1964) 914–915 https://doi.org/10.1038/201914a0.

[55] C.D. Rabadia, Y.J. Liu, G.H. Cao, Y.H. Li, C.W. Zhang, T.B. Sercombe, H. Sun, L.C. Zhang, High-strength β stabilized Ti-Nb-Fe-Cr alloys with large plasticity, Mater. Sci. Eng., A 732 (2018) 368–377 https://doi.org/10.1016/j.msea.2018.07.031.

[56] C.D. Rabadia, Y.J. Liu, L. Wang, H. Sun, L.C. Zhang, Laves phase precipitation in Ti-Zr-Fe-Cr alloys with high strength and large plasticity, Mater. Des. 154 (2018) 228–238 https://doi.org/10.1016/j.matdes.2018.05.035.

[57] J.C. Wang, S.X. Liang, Z. Jia, W.C. Zhang, W.M. Wang, Y.J. Liu, J. Lu, L.C. Zhang, Chemically dealloyed Fe-based metallic glass with void channels-like architecture for highly enhanced peroxymonosulfate activation in catalysis, J. Alloy. Comp. 785 (2019) 642–650 https://doi.org/10.1016/j.jallcom.2019.01.130.

[58] V. Vancauwenberghe, P. Verboven, J. Lammertyn, B. Nicolai, Development of a coaxial extrusion deposition for 3D printing of customizable pectin-based food simulant, J. Food Eng. 225 (2018) 42–52 https://doi.org/10.1016/j.jfoodeng.2018.01.008.

[59] L.J. Zheng, Y.Y. Liu, S.B. Sun, H. Zhang, Selective laser melting of Al-8.5Fe-1.3V-1.7Si alloy: investigation on the resultant microstructure and hardness, Chin. J. Aeronaut. 28 (2015) 564–569 https://doi.org/10.1016/j.cja.2015.01.013.

[60] P. Manda, U. Chakkingal, A.K. Singh, Hardness characteristic and shear band formation in metastable β-titanium alloys, Mater. Char. 96 (2014) 151–157 https://doi.org/10.1016/j.matchar.2014.07.027.

[61] X. Fu, M. Guojun, Z. Xinqing, X. Huibin, Effects of Nb content on yield strength of NiTiNb alloys in martensite state, Chin. J. Aeronaut. 22 (2009) 658–662 https://doi.org/10.1016/S1000-9361(08)60155-7.

[62] S.N. Saud, R. HosseinianS, H.R. Bakhsheshi-Rad, F. Yaghoubidoust, N. Iqbal, E. Hamzah, C.H.R. Ooi, Corrosion and bioactivity performance of graphene oxide coating on TiNb shape memory alloys in simulated body fluid, Mater. Sci. Eng., C 68 (2016) 687–694 https://doi.org/10.1016/j.msec.2016.06.048.

[63] Y.F. Zheng, B.L. Wang, J.G. Wang, C. Li, L.C. Zhao, Corrosion behaviour of Ti–Nb–Sn shape memory alloys in different simulated body solutions, Mater. Sci. Eng., A 438–440 (2006) 891–895 https://doi.org/10.1016/j.msea.2006.01.131.

[64] R. Chelariu, G. Bolat, J. Izquierdo, D. Mareci, D.M. Gordin, T. Gloriant, R.M. Souto, Metastable beta Ti-Nb-Mo alloys with improved corrosion resistance in saline solution, Electrochim. Acta 137 (2014) 280–289 https://doi.org/10.1016/j.electacta.2014.06.021.

[65] J.C. Wang, Z. Jia, S.X. Liang, P. Qin, W.C. Zhang, W.M. Wang, T.B. Sercombe, L.C. Zhang, $Fe_{73.5}Si_{13.5}B_9Cu_1Nb_3$ metallic glass: rapid activation of peroxymonosulfate towards ultrafast Eosin Y degradation, Mater. Des. 140 (2018) 73–84 https://doi.org/10.1016/j.matdes.2017.11.049.

[66] Z. Jia, X. Duan, P. Qin, W. Zhang, W. Wang, C. Yang, H. Sun, S. Wang, L.-C. Zhang, Disordered atomic packing structure of metallic glass: toward ultrafast hydroxyl radicals production rate and strong electron transfer ability in catalytic performance, Adv. Funct. Mater. 27 (2017) 1702258 https://doi.org/10.1002/adfm.201702258.

[67] B.L. Wang, Y.F. Zheng, L.C. Zhao, Electrochemical corrosion behavior of biomedical Ti–22Nb and Ti–22Nb–6Zr alloys in saline medium, Mater. Corros. 60 (2009) 788–794 https://doi.org/10.1002/maco.200805173.

[68] S.-X. Liang, Z. Jia, Y.-J. Liu, W. Zhang, W. Wang, J. Lu, L.-C. Zhang, Compelling rejuvenated catalytic performance in metallic glasses, Adv. Mater. 30 (2018) 1802764 https://doi.org/10.1002/adma.201802764.

[69] A.C. Alves, F. Wenger, P. Ponthiaux, J.P. Celis, A.M. Pinto, L.A. Rocha, J.C.S. Fernandes, Corrosion mechanisms in titanium oxide-based films produced by anodic treatment, Electrochim. Acta 234 (2017) 16–27 https://doi.org/10.1016/j.electacta.2017.03.011.

[70] D. Doraiswamy, S. Ankem, The effect of grain size and stability on ambient temperature tensile and creep deformation in metastable beta titanium alloys, Acta Mater. 51 (2003) 1607–1619 https://doi.org/10.1016/S1359-6454(02)00561-X.

[71] Y. Lee, M. Nordin, S.S. Babu, D.F. Farson, Effect of fluid convection on dendrite arm spacing in laser deposition, Metall. Mater. Trans. B 45 (2014) 1520–1529 https://doi.org/10.1007/s11663-014-0054-7.

[72] C.D. Rabadia, Y.J. Liu, S.F. Jawed, L. Wang, Y.H. Li, X.H. Zhang, T.B. Sercombe, H. Sun, L.C. Zhang, Improved deformation behavior in Ti-Zr-Fe-Mn alloys

comprising the C14 type Laves and β phases, Mater. Des. 160 (2018) 1059–1070 https://doi.org/10.1016/j.matdes.2018.10.049.

[73] S. Ehtemam-Haghighi, G. Cao, L.-C. Zhang, Nanoindentation study of mechanical properties of Ti based alloys with Fe and Ta additions, J. Alloy. Comp. 692 (2017) 892–897 https://doi.org/10.1016/j.jallcom.2016.09.123.

[74] K.M. Flores, W.L. Johnson, R.H. Dauskardt, Fracture and fatigue behavior of a Zr–Ti–Nb ductile phase reinforced bulk metallic glass matrix composite, Scripta Mater. 49 (2003) 1181–1187 https://doi.org/10.1016/j.scriptamat.2003.08.020.

[75] M.-K. Han, J.-Y. Kim, M.-J. Hwang, H.-J. Song, Y.-J. Park, Effect of Nb on the microstructure, mechanical properties, corrosion behavior, and cytotoxicity of Ti-Nb alloys, Materials 8 (2015) 5986–6003 https://doi.org/10.3390/ma8095287.